CIMAC CONGRESS 25
ZURICH, MAY 19 – 23, 2025

2025 | 197

CFD simulations of prechamber gas engines with temporal adjustment of turbulent flame speed

Simulation Technologies, Digital Twins and Complex System Simulation

Azusa Fuse, Mitsubishi Heavy Industries

Daisuke Takemoto, Mitsubishi Heavy Industries, Ltd.
Yoshitane Takashima, OSAKA GAS CO.,LTD.
Yusuke Imamori, Mitsubishi Heavy Industries, Ltd.
Tomohiro Noguchi, Mitsubishi Heavy Industries Engine & Turbocharger, Ltd.
Takahiro Sako, OSAKA GAS CO.,LTD.
Masashi Katsuki, Osaka University

ABSTRACT

To increase the thermal efficiency of prechamber gas engines, optimization of heat release rate in a combustion chamber, and an expansion of knock margin are needed. For the investigation, the use of three dimensional CFD simulations is spreading. However, it is necessary to implement adequate physical models to predict jet ignition and early combustion dynamics in a main chamber.

In this research, three dimensional CFD simulations of a prechamber gas engine for power generation with different prechamber hole geometries such as number of holes, hole diameter, were conducted. To evaluate heat release characteristics of jet ignition and flame propagation from jet flame, CFD results were compared with corresponding experimental results in terms of apparent heat release rate in a main chamber, and flame luminosity of a main chamber near exhaust valve region.

RANS simulations using G-equation combustion model with Peters turbulent flame speed model were conducted. When jet flames penetrated into a main chamber, turbulent combustion condition temporally shifted to broken reaction zones (BRZ) in Peters regime diagram. In the BRZ, flame quenches and flame surfaces may not be defined, which means it may be difficult to use G-equation model which solves the propagation of a consecutive iso-surface of a scalar value. Thus, turbulent flame speed model constant which adjusts degree of flame speed enhancement by turbulence were changed according to turbulent combustion condition to suppress flame surface propagation and to recover afterwards.

The aforementioned model treatment was adapted to CFD simulations of different prechamber hole geometries which make the time when jet flames are classified in BRZ different. The CFD reproduced the changing tendency of initial heat release rate in a main chamber due to jet ignition and transition timings from jet ignition to flame propagation. As for local flame characteristics, the tendency of flame displacement speed and flame width by the change of nozzle geometries were not reproduced by CFD.

The CFD technique mentioned above can be adapted to the investigation of engine performance as a whole, and can be extended to larger size or higher power engines. Thus, we will expand its use as a common technique among our product lineup and will accelerate our product development process, and further improvements of CFD technique will be considered in the future work.

1 INTRODUCTION

Knocking is one of the main factors hindering efficiency improvement of internal combustion engines, and countermeasures for an increase of knock margin has been investigated. In this process, use of CFD (Computational Fluid Dynamics) is becoming important to predict effects of countermeasures in advance. However, for highly accurate prediction, physical models to reproduce phenomena are necessary. In gas engines with prechamber, jet flames ejected from prechamber nozzle ignite fuel-air mixture in main chamber at multiple points, which enhances combustion in main chamber. Thus, in CFD of gas engines with prechamber, adequate physical models to predict dynamics of prechamber jet flames are crucial.

Many studies using high-fidelity simulation methodologies such as LES (Large Eddy Simulation) or DNS (Direct Numerical Simulation) which incorporate fine computational mesh with detailed chemical reaction calculation has been carried out to understand phenomena. Kimura, *et al*.[1] conducted LES of jet flames with different mixture conditions to study ignition characteristics in main chamber, and attempted to organize ignition map based on characteristics of jet flames. Male, *et al.*[2] conducted DNS of jet flames with different ejection velocity and inlet temperature of jet flames to study effects on flame structures, and constructed a model to predict whether ignition occurs or not. On the other hand, these simulation methodologies are costly for CFD of industrial engines, and physical models for CFD which has less computational cost, such as RANS (Reynolds Averaged Navier-stokes) simulation, has not been fully developed.

In this paper, CFD of prechamber gas engine is conducted and combustion modeling for prechamber jet flames is investigated by focusing on transition of turbulent combustion conditions. CFD results with different prechamber nozzle geometries are compared with corresponding experimental results.

2 3-DIMENSIONAL CFD FOR PRECHAMBER GAS ENGINES

2.1 Target engine

Fig. 1 shows an external view of a prechamber gas engine and shape of a prechamber which are used for CFD. Fuel is supplied to a main chamber with intake air, and is directly supplied to the prechamber as well. 3 types of prechamber nozzle geometries which are shown in Table 2 are considered. Prechamber volume is the same, and total area of the prechamber nozzles is different with different nozzle diameter and the number of nozzles. There are two intake and exhaust valves, but in this study, one of the exhaust valves is replaced with a bore scope was installed to visualize the inside of main chamber as in Fig. 2.

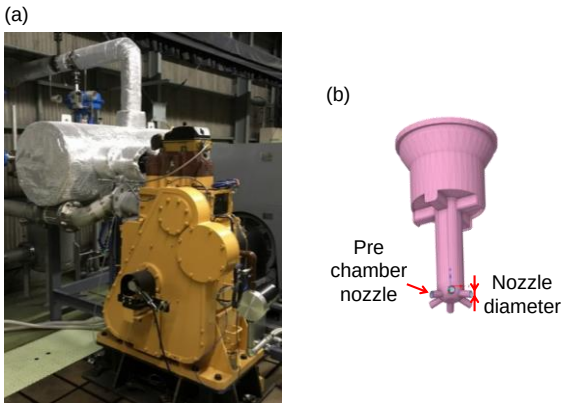

Figure 1. External view of (a) prechamber gas engine and (b) prechamber.

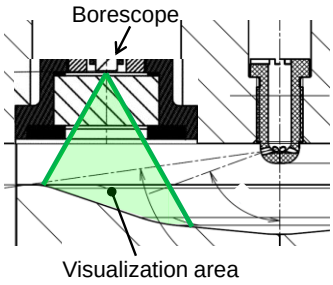

Figure 2. Visualization area by a bore scope.

Table 1. Engine specifications.

Item	Value
Bore/Stroke	160/220mm
Compression ratio	12.0
BMEP/Rotational speed	1.2MPa/1200rpm
Fuel	13A
Fuel supply method	Prechamber: Direct supply Main chamber: Premixed with intake air

Table 2. Prechamber nozzle specifications.

Item	Unit	Type1: Φ1.9-4N	Type2: Φ1.9-6N	Type3: Φ3.9-4N
Nozzle diameter	mm	1.9	1.9	3.9
The number of nozzles	-	4	6	4
Total cross-sectional area of nozzles	mm^2	11.3	17.0	47.8

2.2 CFD methodology

RANS simulation with RNG (Renormalization Group) *k-ε* turbulence model is conducted. As for combustion, G-equation model[3] is used. In the model, under an assumption that flame thickness is very thin compared to turbulent eddy scale, flame propagation can be expressed by movement of a flame surface by solving time evolution of the transport equation of the scalar *G* iso-surface (Eq. 1). By using this model, although very fine computational mesh will be needed within flame thickness to reproduce chemical reactions in flame, coarser mesh can be used, which make computational cost affordable. However, the turbulent burning velocity S_T appeared in the second term on the right side of Eq. 1 needs to be modeled. In this study, the model of Peters[3] is used (Eq. 2), where S_L, u'_{rms}, and *Da* are the laminar burning velocity, the turbulence intensity, and the Damkohler number, respectively. a_4, b_3, and b_1 are model parameters. In a conventional way, values are fixed during simulation as a_4=0.78, b_3=1.0, and b_1=2.2 for prechamber and 1.4 for main chamber.

$$\frac{\partial \rho \tilde{G}}{\partial t} + \frac{\partial \rho \widetilde{u_i} G}{\partial x_i} = -\rho D_t \tilde{\kappa} \left|\frac{\partial \tilde{G}}{\partial x_i}\right| + \rho_u S_T \left|\frac{\partial \tilde{G}}{\partial x_i}\right| \quad (1)$$

$$S_T = S_L + u'_{rms}\left(-\frac{a_4 b_3^2}{2b_1} Da + \sqrt{\left(\frac{a_4 b_3^2}{2b_1} Da\right)^2 + a_4 b_3^2 Da}\right) \quad (2)$$

To make computational cost much less, refinement of mesh is limited to focused regions. The adaptive mesh refinement is applied to dynamically refine mesh only in the region where temperature and velocity gradient are steep. In addition to that, to suppress the effect of numerical diffusion on penetration of jet flames, mesh in area where jet flames penetrate are refined.

3 COMBUSTION MODELING ACCORDING TO TURBULENT COMBUSTION CONDITIONS

3.1 Turbulent combustion condition of jet flames

First, the turbulent combustion conditions of jet flames are analyzed. Fig. 3 shows the comparison between CFD and experimental results with nozzle type2: Φ1.9-6N. While the timing and its value of the first local maxma of prechamber pressure p_{pre} is well predicted, the timing of the maximum of main chamber pressure p_{main} is earlier than the experimental result. This results from the overprediction of heat release rate in main chamber $ROHR_{main}$ from -3 to 5 deg.ATDC. The timing where $ROHR_{main}$ starts to increase is well predicted. However, the rate of $ROHR_{main}$ increase is overpredicted in CFD. In the experimental result, $ROHR_{main}$ stagnates around TDC timing with its value of 0.3 kJ/deg, and increases again after that. Although the aforementioned trend is reproduced in the CFD result, the $ROHR_{main}$ value 0.45 kJ/deg where it stagnates is higher and the duration of stagnation is shorter than the experimental result.

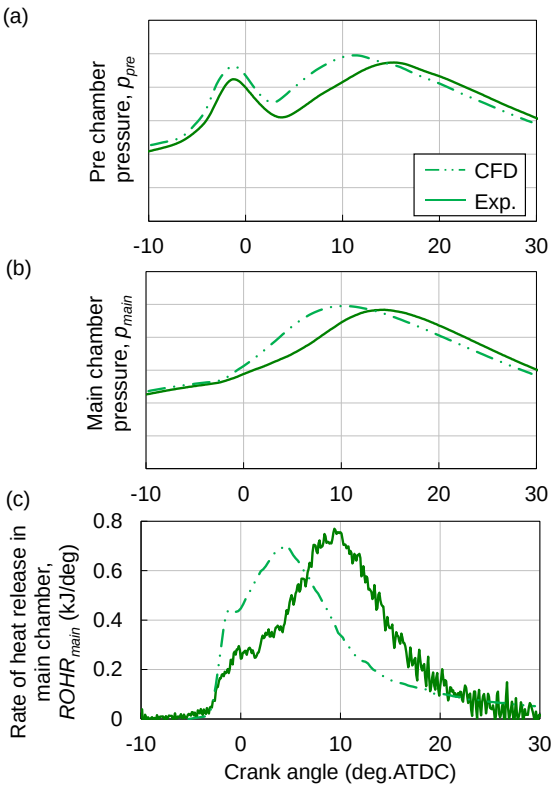

Figure 3. Temporal evolution of (a) Prechamber pressure P_{pre}, (b) main chamber pressure P_{main}, and (c) rate of heat release in main chamber $ROHR_{main}$ with prechamber nozzle type2: Φ1.9-6N.

To analyze the turbulent combustion conditions, spatial variations of the temperature, the velocity, and the turbulent Karlovitz number Ka_t in the cross-sectional area of the main chamber are shown in Fig. 4. Here, Ka_t is calculated using the Kolmogorov velocity v_k and S_L as

$$Ka_t = \left(\frac{v_k}{S_L}\right)^2 \quad (3)$$

At -2.5 deg.ATDC when the jet flames ejected to the main chamber, high Ka_t region (Ka_t>100) exists near nozzles. From -1.5 to 0.5 deg.ATDC when $ROHR_{main}$ stagnates, while the region with high Ka_t

remains, the region with relatively low Ka_t expands as flame tips propagate. Subsequently, at 2.0 deg.ATDC when the ejection of jet flames is almost finished, the region with high Ka_t disappeared. The above trend shows that the period of $ROHR_{main}$ stagnation corresponds to the transition from prechamber jet flames to developed propagating flames in the main chamber.

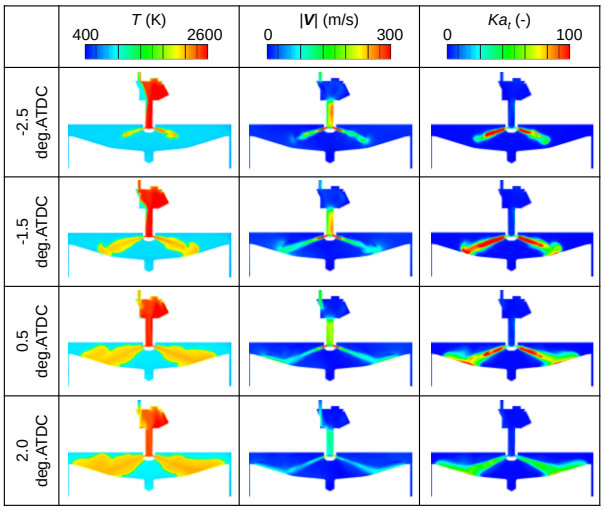

Figure 4. Spatial variations of the temperature T, the flow velocity magnitude $|V|$, and the turbulent Karlovitz number Ka_t in the cross-sectional area in the main chamber with prechamber nozzle type2: Φ1.9-6N.

To understand the aforementioned transition process quantitatively, the temporal evolution of turbulent combustion conditions in Peters diagram[3] is analyzed. As shown in Fig. 5, in Peters diagram, turbulent combustion conditions are classified by 5 different regimes by ratios of length scales and velocities of turbulence and unstrained laminar flame. Here, l_E and δ_F are the turbulent integral length and the laminar diffusive thickness, respectively. These quantities are calculated using properties of unburned mixture. In this study, to focus on the turbulence caused by the jet flames ejection and its effect on flames, unburned area which is located 1 mm away from the flame surface is extracted. In Fig. 5, the turbulent combustion conditions in each crank angle timing between -3 to 10 deg.ATDC are shown. The symbols denote the mean of the CFD result in each crank angle timing and the error bars in horizontal and vertical directions show the standard deviations of l_E/δ_F and u'_{rms}/S_L, respectively. At -3 deg.ATDC when jet flames started to eject to the main chamber, the symbol locates near the boundary between the broken reaction zones and the thin reaction zones, and then moves down to the right. In the broken reaction zones, there may be no continuous flame surfaces, since strong turbulent motions fragments flame surfaces[3]. In this regime, the G-equation model (Eq. 1) and the Peters' model for S_T (Eq. 2) are not applicable, since they assume continuous surface propagation. Therefore, the discrepancy between the CFD and the experimental results or $ROHR_{main}$ in Fig. 2 is due to failure of reproduction of combustion in broken reaction zones and subsequent transition to propagating flames. In the next section, the model correction method to reproduce the transition process is described.

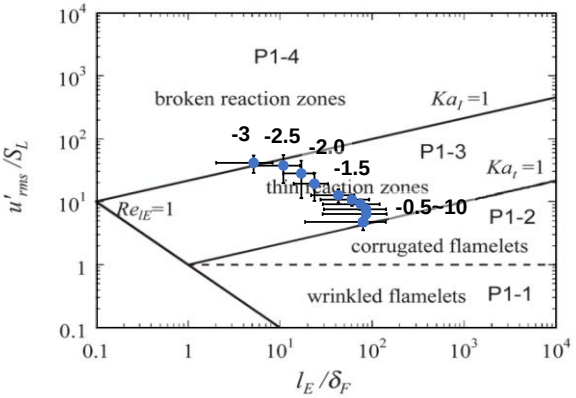

Figure 5. Temporal evolution of turbulent combustion conditions in Peters diagram[3].

3.2 Examination of the turbulent combustion speed correction method according to the combustion condition

In this section, the methodology to take into account effects of strong turbulent motions on flames in the context of the G-equation model are discussed. Fig. 6 shows the relationship between S_T/S_L and u'_{rms}/S_L. While S_T/S_L increases with an increase of u'_{rms}/S_L up to 10, more increase of u'_{rms}/S_L causes flame extinction. Since u'_{rms}/S_L is the value of vertical axis in the Peters diagram, flame extinction in Fig. 6 may correspond to the transition to the broken reaction zones. In other words, in the broken reaction zones, the effect of u'_{rms}/S_L on S_T/S_L should be considered differently compared to other turbulent combustion conditions to reproduce this non-linear phenomenon.

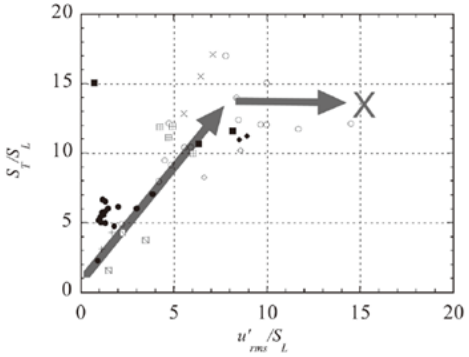

Figure 6. Relationship between S_T/S_L and u'_{rms}/S_L.[4]

In the Peters' model for S_T (Eq. 2), the parameter b_1 originally plays a role in adjusting the degree of the effect of u'_{rms} on S_T. Thus, it may be appropriate to adjust b_1 value. However, when b_1 value is set constant during simulation, CFD cannot reproduce $ROHR_{main}$ in both the transition period (around 0 deg.ATDC) and the subsequent phase as shown in Fig. 7. Therefore, time variations of b_1 value should be given.

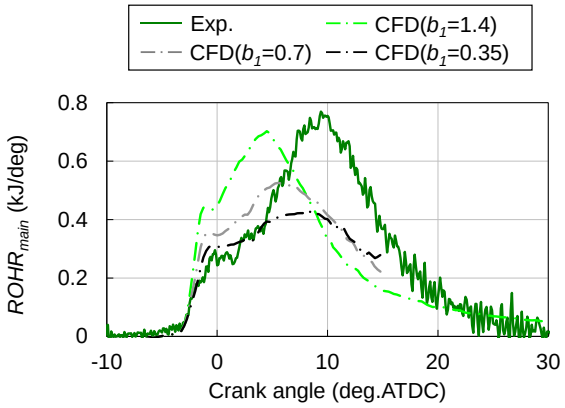

Figure 7. Temporal evolution of $ROHR_{main}$ of CFD results with different b_1 values with prechamber nozzle type2: Φ1.9-6N.

In this study, the following method is proposed.

$$b_1 = b_{1,BRZ} \cdot \alpha_{BRZ} + b_{1,flm} \cdot (1.0 - \alpha_{BRZ}) \qquad (4)$$

The value of b_1 is calculated by Eq. 4 *on-the-fly*, and the same values are set for all computational cells in the main chamber. Here, $b_{1,BRZ}$ and $b_{1,flm}$ are b_1 in broken reaction zones which is set to 0 and in other regimes which is set to 1.4, respectively. α_{BRZ} is a ratio of unburned mixture volume in broken reaction zones to the total unburned mixture volume of interest which is the same as in the Peters diagram. When Ka_t of each computational cell in unburned mixture is above 100, the cell is classified as the broken reaction zones. Here, Ka_t is corrected from Eq. 3, as

$$Ka_t = \left(\frac{v_k}{S_L}\right)^2 \cdot \frac{\varepsilon}{\langle\varepsilon\rangle} \cdot Const \qquad (5)$$

where ε is turbulent energy dissipation rate, <> is an average in the total unburned mixture volume, and *Const* is the model constant which is set to 50 in this study. Eq. 3 is corrected by ε to consider the effect of strain on local S_L.

S_L in Eq. 3 is normally the value of unstrained laminar flame. However, when flames are subjected to strain which can be seen in jet flames as illustrated in Fig. 8, local S_L changes and flames extinguish with strong strain. These interactions between flames and flows can be examined by using results of high-fidelity simulation method which can solve transportation of mass and heat with high precision. However, CFD settings in this study are not enough to reproduce these phenomena. Thus, the way to consider this interaction is needed. According to Cant *et al.*[5], strain rate is correlated with vortex motions at the Kolmogorov scale level. Here, the Kolmogorov length scale is expressed as $(\varepsilon\nu)^{1/4}$ by using ε and kinematic viscosity, ν, thus the strain rate is considered to be proportional to ε. Thus, Ka_t is corrected by using ε, as in Eq. 5. The validity of this method is verified in the next section.

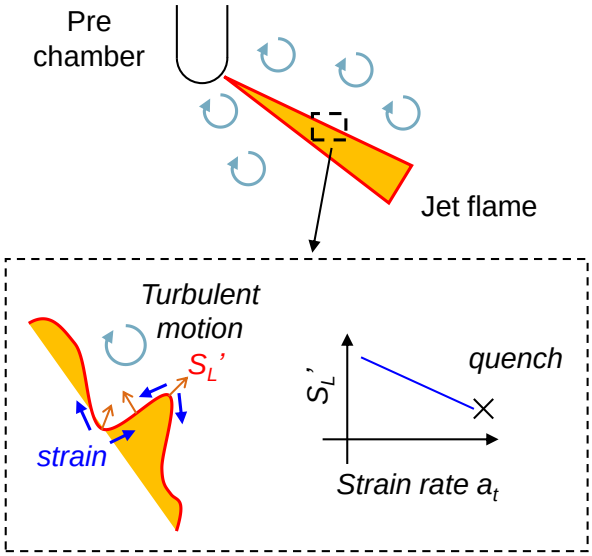

Figure 8. Schematics of the effect of turbulent motions on local S_L.

4 RESULTS

First, the proposed S_T adjustment method using Eq. 4 and 5 is compared with the conventional method (no time variations of b_1). Fig. 9 shows the comparison of $ROHR_{main}$ of nozzle type2: Φ1.9-6N. By using the proposed method, deviations of $ROHR_{main}$ in both transition period (around 0 deg.ATDC) and subsequent phase between the CFD and the experimental results are decreased. The proposed method is further adapted to CFD with different prechamber nozzle geometries. Fig. 10 shows the comparison of $ROHR_{main}$. Here, only CFD results with the proposed method are shown. Changes by different nozzle geometries in terms of $ROHR_{main}$ around 0 deg.ATDC, and the maximum of $ROHR_{main}$ and its timing are captured well by CFD. This suggests that the proposed method can capture the transition process in the main chamber. On the other hand, the maximum value of $ROHR_{main}$ itself is underpredicted for all nozzle geometries.

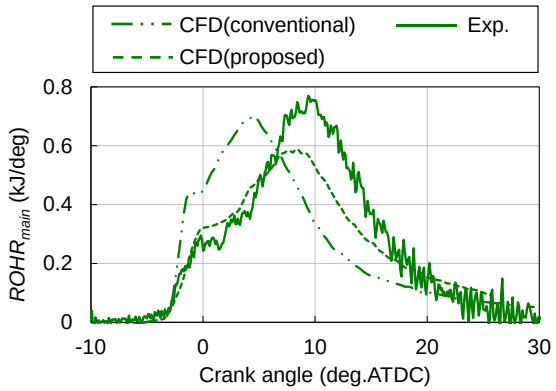

Figure 9. Comparison of $ROHR_{main}$ between the experimental result and results of CFD with the conventional and the proposed methods with prechamber nozzle type2: Φ1.9-6N.

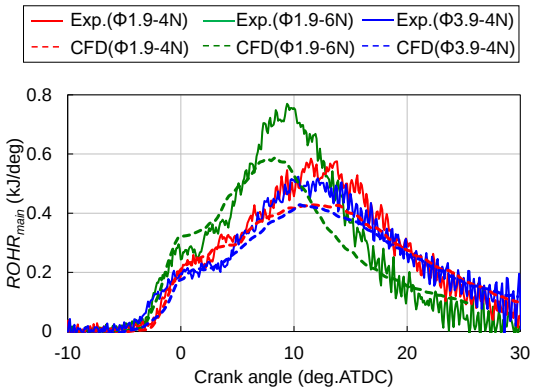

Figure 10. Comparison of $ROHR_{main}$ between the CFD with the proposed method and the experimental results with different prechamber nozzle geometries.

Besides the mean characteristic in main chamber, local characteristics are analysed by using flame visualization images near exhaust valve as in Fig. 2. Fig. 11 shows the temporal evolution of flame surfaces of the experimental results. The image taken by a high-speed camera is amplified by an image intensifier, and flame surfaces are extracted from binarized images. The prechamber nozzle exit is located at lower-right corner, and jet flames moves up to the left. Flame surfaces are bounded by circle in late timings since the visualization area is circle from the top view. With nozzle type1: Φ1.9-4N, flame surfaces reaches to upper-left corner at 5.2 deg.ATDC, which is the earliest among 3 nozzle geometries. Besides, with the total cross-sectional area of nozzles increase from type1: Φ1.9-4N to type3: Φ3.9-4N, flame width is getting larger. In Fig. 12, the temporal evolution of flame surfaces of the CFD results are shown. Flame surfaces are defined as T=1500K iso-surfaces. In CFD results, flame surfaces propagate fastest with type2: Φ1.9-6N, and no clear differences in flame width between different nozzle geometries. These results suggests that current CFD method can be adapted to the analysis of engine performance as a whole; however, when one have to examine the local phenomena such as understanding the cause of knocking by focusing on local flame surfaces and velocity distributions[6], current method can mislead the investigations. In this sense, further improvement will be needed, and the aforementioned discrepancies are analyzed.

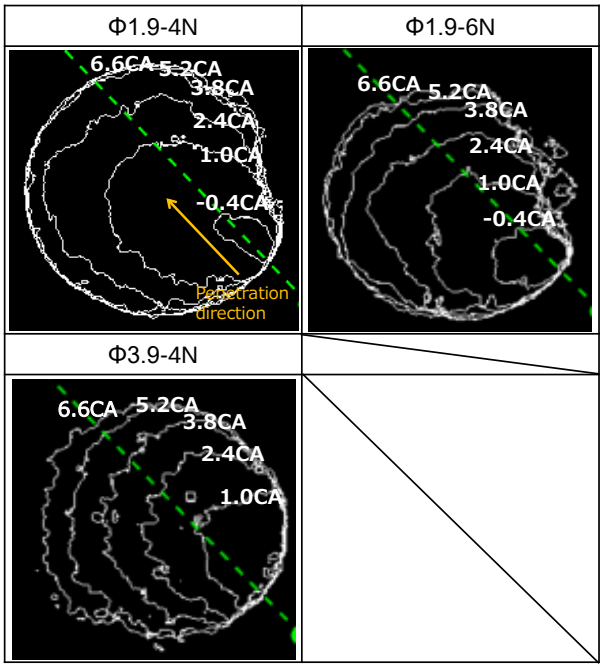

Figure 11. Experimental results of flame surfaces evolution.

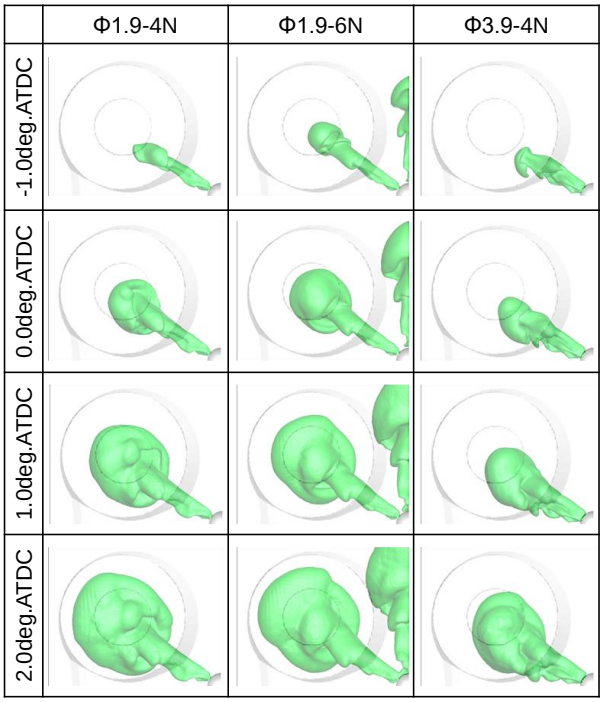

Figure12. CFD results of flame surfaces evolution.

First, the arrival timing of flame surfaces is analyzed by separating into 2 stages which are stage1. the period when jet flames ejected from nozzles, and stage2. the timing when jet flames impinged to the piston wall.

As for the stage1, pressure difference between main chamber and prechamber are analyzed, since it drives the jet flames to eject, and affect to the ejection velocity. In Fig.13, the comparison of pressure difference with different prechamber nozzle geometries are shown. The CFD result with nozzle type2: Φ1.9-6N overpredicts the maximum value and deviation from experimental result is largest. This may cause the overprediction of ejection velocity of jet flames.

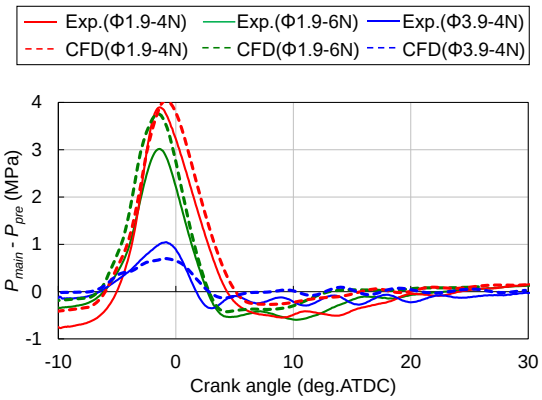

Figure 13. Comparison of main chamber and prechamber pressure difference P_{main}-P_{pre} between the CFD and the experimental results with different prechamber nozzle geometries.

As for the stage2, flame displacement speed near the impingement timing is examined. In Fig. 14, flame displacement speed at axial position in flame penetration direction are shown. The displacement speed is calculated over the line which is shown as green dashed line in Fig. 11. In CFD results, flames impinged at around 30 mm position, which corresponds to 440 pixel position in experimental results. In the experimental results with nozzle type1: Φ1.9-4N, there is an increase of displacement speed at around 650 pixel position compared to other nozzle geometries. However, this increase is not clearly observed in the CFD results. In Fig. 15, spatial variations of the temperature and the flow velocity vectors are shown. After the impingement, there is a circulation near flame tip which is caused by the impingement. This circulation pushes the flame tip towards the penetration direction and the flame displacement speed may be increased. In other words, absence of the flame speed increment suggests that the prediction of flow after impingement may have some space to be improved.

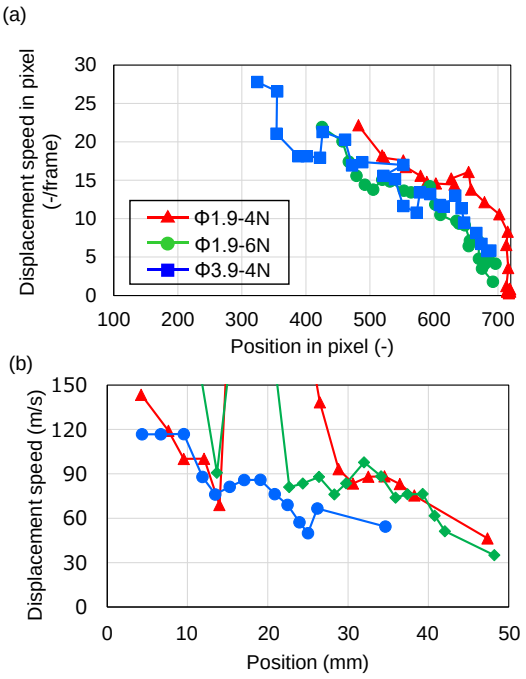

Figure 14. Flame displacement speed at axial position in flame penetration direction of (a) experimental results and (b) CFD results.

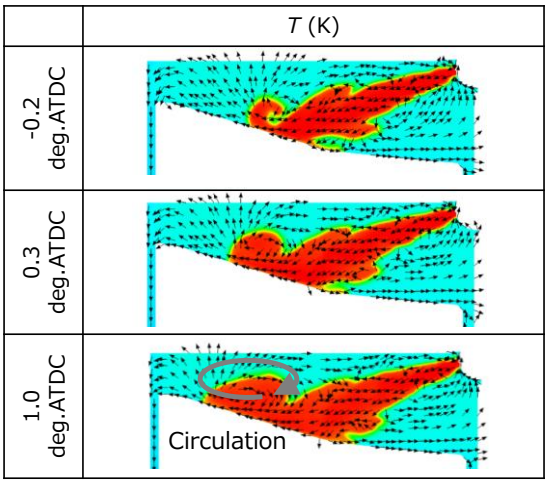

Figure 15. Spatial variations of the temperature and the flow velocity vectors in the cross-sectional area including prechamber nozzle axis with prechamber nozzle type2: Φ1.9-6N.

Second, the flame width is analyzed. Since the ejection velocity near the nozzle is very high (order of 100 m/s) as in Fig. 4, and the directions of velocity vectors are more or less parallel to the nozzle axial direction as in Fig. 15, the flame width may be determined by the flame propagation towards nozzle axial vertical direction, which

seems to be very slow. In this study, turbulent combustion conditions are focused; however, thermo-chemical conditions of jet flames itself near nozzle exit are affected by temperature decrease due to heat loss inside the nozzles[7], and absence of radicals near nozzle exit[8] and etc., as well, which is out of scope in this study. Taking into account these phenomena can contribute to the improvement of the prediction of flame width. In addition to this, in the proposed S_T adjustment method, all computational cells have the same b_1 value regardless of local turbulent combustion conditions, which can not fully reproduce the spatial variations of S_T. Therefore, the method to change b_1 according to the local combustion condition in a pointwise manner can also contribute to the improvement of the prediction of flame width.

5 CONCLUSIONS

RANS simulation of the prechamber gas engine was conducted to analyze turbulent combustion conditions of jet flames. At the beginning of jet flame ejection, the turbulent combustion conditions were classified as the broken reaction zones. Rate of heat release in the main chamber after jet flame ejection and at subsequent transition period from jet flames to developed propagating flames were overestimated by CFD. This was due to that the G-equation combustion model is not applicable since it cannot reproduce the local fragmentation event of flame surfaces in the broken reaction zones. Thus, the method of adjusting model parameter according to the turbulent combustion conditions were proposed. The model calculated parameter value using the instantaneous volume ratio of unburned mixture classified as the broken reaction zones to the total unburned mixture of interest. Local turbulent Karlovitz number which was corrected by strain rate effect was used for the classification.

CFD with the proposed method for 3 types of prechamber nozzle geometries with different nozzle diameter and the number of nozzles was conducted to validate the model. The comparison with the CFD and the corresponding experimental results showed that the CFD succeeded to capture the temporal evolution of rate of heat release in the main chamber. In addition, local flame characteristics were analyzed by comparing with experimental results of flame visualization images near exhaust valve. The comparison showed that the tendency of flame displacement speed and flame width by the change of nozzle geometries were not reproduced by CFD. These results suggested that the proposed method can be adapted to the analysis of engine performance as a whole; however, further improvement will be needed for the investigation of local phenomena such as understanding the cause of knocking. For the improvement, prediction of pressure difference between the main chamber and prechamber, flow after jet flame impingement to the wall, local thermos-chemical state near the nozzles, and spatial variations of model parameter are identified as items.

6 REFERENCES

[1] Kimura, M., Suzuki, K., Suzuki, N., Morikawa, K., Tanoue, K., Kuboyama, T., Moriyoshi, Y. 2023. Numerical Study on Main chamber Ignition and Combustion Mechanisms by Prechamber Hot Gas Jet, *The 34th Internal Combustion Engine Symposium*, Japan, 20234634.

[2] Male, Q., Vermorel, O., Ravet, F., and Poinsot, T. 2021. Direct numerical simulations and models for hot burnt gases jet ignition, *Combustion and Flame*, 223, 407-422.

[3] Peters, N., 2000. *Turbulent Combustion*, COMBRIDGE UNIVERSITY PRESS, Cambridge, UK.

[4] Tanahashi, M. 2009. Turbulent Premixed Combustion I -Reference Scales of Turbulence and Premixed Flame-, *Journal of the Combustion Society of Japan*, 51(158), 295-302.

[5] Cant, R. S., Pope, S. B., and Bray, K. N. C. 1990. Modelling of flamelet surface to volume ratio in turbulent premixed combustion, *International Symposium of Combustion Institute*, 23, 809-815.

[6] Suzuki, K., Nomura, K., Fuse, A., Oda, Y., Yamada, S., Yamamoto, T., Tsujimura, T., and Suzuki, Y. 2024. Prediction of Knocking Frequency of Hydrogen Fuel Engine by Continuous Cycle Analysis Using CHT-LES, *The 35th Internal Combustion Engine Symposium*, Japan.

[7] Benekos, S., Frouzakis, C. F., Giannakopoulos, G. K., Altantzis, C., and Boulouchos, K. 2021. A 2-D DNS study of the effects of nozzle geometry, ignition kernel placement and initial turbulence on prechamber ignition, *Combustion and Flame*, 225, 272-290.

[8] Sadanandan, R., Markus, D., Schieβl, R., Maas, U., Olofsson, J., Seyfried, H., Richter, M., and Alden, M. 2007. Detailed investigation of ignition by hot gas jets, *Proceedings of the Combustion Institute*, 31, 719-726.